Subaqueous clinoforms created by sandy wave-supported gravity flows: lessons from the central California shelf

Elisa Medri[1], Alexander R. Simms[1], Jared Kluesner[2], Samuel Y. Johnson[2], Stuart P. Nishenko[3], H. Gary Greene[4] and James E. Conrad[2]

[1] University of California, Santa Barbara, Santa Barbara, CA, USA
[2] U.S. Geological Survey, Santa Cruz, CA, USA
[3] Pacific Gas and Electric, San Francisco, CA, USA
[4] Moss Landing Marine Laboratories, CA, USA

Corresponding Author:
Elisa Medri
emedri@ucsb.edu

Abstract

Subaqueous clinoforms are an important shelf feature. Their origins are typically associated with subaerial deltas but recent work has identified similar features in settings without a significant fluvial source (Mitchell, 2012; Patruno et al., 2015; Patruno and Helland-Hansen, 2018). These other studies have shown that such subaqueous clinoforms, also known as infralittoral prograding wedges (IPWs), are created largely by wave-induced processes. This study uses geophysical, sedimentological, and radiocarbon data to determine the sedimentary characteristics and genesis of a shore-parallel subaqueous clinoform developed far from any significant river on the central California continental shelf; a sedimentary shelf buildup known locally as the Cross Hosgri Slope. Sediment cores through the clinoformal sedimentary unit reveal that it is composed of beds with an erosive base, overlain by a thin (~ 15 cm) coarsening upward sequence of shelly fine sands transitioning to a fining upward sequence marked by alternating parallel and ripple cross laminated very fine sands. The sedimentary succession is often capped by fine silts that are commonly interbedded with thin very fine sand beds. Radiocarbon dating of shells collected just above the erosive base indicate the subaqueous clinoform initiated progradation ~7 ka, nucleating on an older Younger Dryas relict shoreface. We suggest the Cross Hosgri Slope was created by winter-storm waves mobilizing sands in water depths up to ~ 70 m that transitioned into wave-

supported gravity flows. The wave-supported gravity flows traveled downslope to water depths of up to ~80 m, corresponding to the foot of the subaqueous clinoform. They did not travel beyond this depth as wave influence at these depths is negligible and the shelf gradient is insufficient to maintain movement of the load alone. Our work suggests that wave-supported gravity flows can entrain very fine sands and silts and build subaqueous clinoforms, even in the absence of a significant river source. Furthermore, we provide a facies model for sandy wave-supported gravity flow deposits.

Keywords: Shelf processes; Gravity flows; Pacific Ocean; Sedimentary facies; Holocene; Quaternary stratigraphy

1. Introduction

Subaqueous clinoforms are inclined, basin-dipping strata, generally sigmoidal in shape, with a typical rollover point at water depths up to 60 m (Cattaneo and Steel, 2003; Mitchell, 2012; Patruno et al., 2015; Patruno and Helland-Hansen, 2018; Steel and Olsen, 2002). Subaqueous clinoforms are commonly observed as part of a compound system (Patruno et al., 2015; Patruno and Helland-Hansen, 2018) associated with fluvial-deltaic systems.

Subaqueous clinoforms can also occur in isolation, not connected to fluvial-deltaic systems (Budillon et al., 2022; Fernández-Salas et al., 2009; Hernandez-Molina et al., 2000; Martínez-Carreño et al., 2017). In these cases, the processes responsible for advection of sediment can be different, and mainly dominated by basin dynamics, such as waves, currents, and tides, rather than direct fluvial input (Patruno et al., 2015; Pirmez et al., 1998). Contouritic clinoforms form in areas with little fluvial input, and are mainly driven by bottom currents (Schattner et al, 2020). However, contouritic clinoforms usually occur along the shelf edge and the upper slope, at greater water depths than the ones discussed in this study. Another feeding mechanism are wave-supported gravity flows (WSGFs), capable of moving

large amounts of sediment across continental shelves (Ozdemir, 2016; Traykovski et al., 2007). WSGFs are the result of resuspension of sediment by wave energy, generating a high-density layer near the seabed that moves downslope, and eventually dissipates when wave energy is not sufficient to maintain sediment entrainment (Flores et al., 2018; Ma et al., 2008). On energetic continental shelves, wave influence can create high-density turbulence layers and enough shear stress to remobilize sediments in shallow coastal areas and promote their downslope movement to distal areas of continental shelves (Flores et al., 2018; Ozdemir, 2016; Traykovski et al., 2007; Wright et al., 2001; Wright and Friedrichs, 2006). The literature investigating WSGFs is relatively small, and these processes have mainly been recorded in association with large river floods, mobilizing exclusively mud-sized grains (Ma et al., 2008; Ogston et al., 2000; Scully et al., 2003). While this has been observed on river-derived, fine-grained sediments, Flores et al. (2018) showed that the same conditions can be attained in sandy environments without an associated river flood, indicating that this phenomenon may occur in a wider range of settings than previously reported. Furthermore, while a growing number of papers focus on modeling WSGF processes and dynamics (Ozdemir, 2016; Puig et al., 2003; Scully et al., 2003; Traykovski et al., 2007; Wright et al., 2001; Wright and Friedrichs, 2006), observation of their deposits and associated facies – specifically sandy WSGFs – are rare.

The continental shelf of central California is characterized by a high-energy wave climate (Storlazzi and Wingfield, 2005) and is marked by numerous sandy, coast-parallel to subparallel geomorphic features. One of these is informally known as the Cross Hosgri Slope (CHS), a southwest-facing sandy clinoform located at a water depth of ~70 m and ~2 km from the modern shoreline (Johnson et al., 2014; Fig. 1). Previously collected seismic-reflection data show that it is a subaqueous clinoform (Johnson et al., 2014). The purpose of this study is to describe and interpret the origin of the CHS and its deposits by analyzing

87 cores, high-resolution seismic chirp data, and ^{14}C ages. This study also provides a facies
88 model for WSGF deposits in sandy environments, and could aid in the differentiation of their
89 deposits from other offshore sand bodies such as overstepped barriers, drowned shorefaces,
90 and other forms of sediment gravity flows.

91 **2. Regional setting**

92 *2.1 Waves, climate and watersheds*

93 The study area lies northwest of Estero Point, central California (Fig. 1). The region has a
94 narrow (< 5 km) continental shelf offshore of the coastal Santa Lucia Mountains, which are
95 incised by small, narrow ephemeral and perennial streams. The largest nearby stream is the
96 ephemeral 123 km^2 Santa Rosa Creek watershed, which lies ~10 km north of the CHS. Santa
97 Rosa Creek and the other nearby smaller streams flow unobstructed down steep hills mantled
98 with shallow soils and sparse vegetation (Hawley et al., 2012).

99 The central California coast has a Mediterranean climate, with warm dry summers and
100 cool, wet winters (Bakker and Slack, 1985). The climate is controlled by the North Pacific
101 High, a high-pressure system resting over cold upwelling waters, which deflects storms from
102 reaching the California coast during the summer months (Kämpf and Chapman, 2016).
103 During winter, the Pacific High migrates to the south resulting in relatively high rainfall in
104 California between November and March. Overall, the California coast experiences highly
105 variable annual rainfall depending on storm frequency and magnitude. Mean annual rainfall
106 in the Santa Lucia Range varies between 40 and 150 cm (Ramirez et al., 2020).

107 The central California coast is located in an area characterized by a high energy wave
108 climate (Dingler et al., 1982), where average wave periods recorded at the closest wave buoy
109 northwest of Estero Point can reach 10 s, with mean significant wave heights up to 5-6 m in
110 the winter seasons (NOAA.gov; Storlazzi and Wingfield, 2005). The wave climate in central
111 California is controlled by three main trends: (i) the north Pacific swell generated by cyclones

112 in the northern Pacific Ocean during winter months, (ii) a southern swell, generated by winter
113 storms in the southern hemisphere during the northern hemisphere summer, and (iii) locally
114 wind-driven waves (Storlazzi and Griggs, 2000; Storlazzi and Wingfield, 2005). Storm events
115 in this region are greater during the winter months, specifically in the months of December
116 and January. The north Pacific swell approaches from the west/northwest and is largest in
117 October through May, producing the largest waves to impact this region (2–10 m height)
118 (Storlazzi and Wingfield, 2005). The southern swell is more active in summer months, and
119 approaches the coast from the west/southwest with wave heights between 0.3-3 m.

120 The main ocean current influencing the central California coast is the California
121 Current; a wide, strong offshore current that flows south at a distance of ~100 – 200 km from
122 the modern shoreline (Bray et al., 1999; Chelton, 1984; Collins et al., 2003; Hickey, 1998).
123 The California Current reaches its strongest speeds of ~0.05 m/s at the surface and extends to
124 ~ 500 m depth (Auad et al., 2011; Hickey, 1998). A narrower and weaker northward-flowing
125 surface current develops north of Point Conception (Fig. 1b) at ~15-20 km offshore (Collins
126 et al., 2003), reaching its maximum velocity during the winter months (Auad et al., 2011;
127 Checkley and Barth, 2009; Chelton, 1984; Collins et al., 2003; Hickey, 1998; Reid and
128 Schwartzlose, 1962).

129 Due to California's location on the forebulge of the former Last Glacial Maximum ice
130 sheets (Clark et al., 1978), relative sea level (RSL) at this location has risen continuously
131 since the Last Glacial Maximum (Yousefi et al., 2018). However, the physical constraints on
132 RSL history for the southern California coast are largely limited to the past 10-12 ka (Fig. 2)
133 (Reynolds and Simms, 2015). Over this time period, relative sea level has risen
134 approximately 60 m (Fig. 2).

135 *2.2 Structural setting*

The continental shelf off Estero Point, is a tectonically active region crossed by a series of north-south trending strike-slip faults, the largest of which is the Hosgri fault (Hanson et al., 1995; Johnson et al., 2018, 2014; Johnson and Watt, 2012; Langenheim et al., 2013; Nishenko et al., 2018). The Hosgri fault is part of the distributed right-lateral transform boundary between the Pacific Plate and the Sierran microplate, which include the larger San Andreas Fault to the east of the study area. Johnson et al. (2014) estimated a modern slip rate of 2.6 ± 0.9 mm/yr for the Hosgri fault based on offset of the base of the CHS. Over the last 11 Ma, the Hosgri fault is inferred to have experienced 156 +/- 4 km of slip (Dickinson et al., 2005).

2.3 The Cross Hosgri Slope

The Cross Hosgri Slope (CHS) is a shore-parallel sand body located 5 km northwest of Estero Point in water depths of ~70 m (Fig. 1). Johnson et al. (2014) first described it as a southeast-striking feature, with a height of 7-9 m, a length of 1700 m, and a width of 250-280 m. The feature is characterized by a slope of 1.6° - 2.0° dipping to the SW, a considerably steeper angle than the surrounding seafloor to the northeast and southwest, which dips more gently at 0.4° - 0.6° (Johnson et al., 2014). In the absence of sediment cores and radiocarbon ages, Johnson et al. (2014) interpreted the CHS to be a drowned shoreface paired to a now-eroded sandspit, and inferred a Younger Dryas age (~12,800 to 11,500 yr B.P.) based on the global sea-level curve of Stanford et al. (2011).

3. Material and Methods

3.1 Chirp seismic-reflection survey

From October 18th-24th, 2019, the U.S Geological Survey (USGS) Pacific Coastal and Marine Science Center (PCMSC), in collaboration with Pacific Gas and Electric (PG&E), obtained a total of 450 km of high-resolution chirp data from the central California shelf (Snyder et al., 2022). Six kilometers of these data are used in this study to examine the CHS.

These consist of 2 chirp lines, one crossing perpendicular to the CHS (HFC-05), and one parallel to the CHS (HFC-25). The high-resolution seismic survey was conducted aboard the M/V *Bold Horizon* using an Edgetech 2300-516 chirp sub bottom profiler. Chirp data were imported in Shearwater Reveal software and processed using the real (non-Hilbert transformed) traces and included navigation conversion, fish depth correction, multi-step well correction, predictive deconvolution, water column mute, and gain adjustment. The water depths of the survey varied between 30 and 200 m.

3.2 Sediment cores

Seven vibracores ranging in length from ~0.5 - 3.0 m were also collected from the CHS from the M/V *Bold Horizon* using a Rossfelder P-5 vibracore system. A transect of 3 core sites was collected perpendicular across the CHS and in line with one of the chirp profiles (Table 1; Fig. 1). Each of these sites was sampled with a pair of duplicate cores, one for sedimentary characteristics and radiocarbon data, the other in black photo-resistant liner for Optically Stimulated Luminescence dating (OLS) for a subsequent study. Each whole core was scanned using a CT (Computed Tomography) scanner to view internal sedimentary structures, while split core sections were photographed.

3.3 Grain size analysis

Four sediment cores were sampled for grain size analysis, which was conducted using a CILAS 1190L particle size analyzer following the methods of Sperazza et al. (2004). Cores HF-1, HF-3, and HF-7 were sampled at 5 cm intervals, excluding shell hash beds, where the particle size (>2500 μm) was too large for the instrument. HF-5, the longest core, was sampled at 2 cm intervals. The 1 cm^3 samples were pre-treated with 30% hydrogen peroxide (H_2O_2) to remove organic material. Quantification of shell material was performed by pre-weighing dried 1 cm^3 samples collected at intervals of 10 cm, treating them with 10% HCl, and weighing after the reaction was carried out.

186 *3.4 Radiocarbon dating*

187 A total of 30 samples were collected for radiocarbon dating. Of these, 23 were gastropod
188 shells, one was a bivalve, and six were wood fragments. The bivalve was articulated and only
189 gastropods that showed no evidence of reworking, such as abrasion or fragmentation, were
190 sampled. The species of the gastropods were also used to assess their habitat. Radiocarbon
191 ages were measured using atomic mass spectrometry (AMS) at the University of California
192 Irvine Keck carbon cycle accelerator mass spectrometer (KCCAMS) facility. Radiocarbon
193 ages obtained from shells were calibrated using the Marine 20 calibration curve of (Heaton et
194 al., 2020), while wood fragments were calibrated using the Intcal calibration curve of
195 (Reimer et al., 2020) within the Calib 8.2 program (Stuiver et al., 2022).

196 **4. Results**

197 *4.1 Sedimentary facies*

198 Sediments collected from the CHS consist of silt, very fine sand, and fine sand (average
199 grain sizes ranging from 80 – 130 μm) (Fig. 3). All sedimentary facies contain shell
200 fragments, which range in size from 0.2 mm to 5 cm, and several of the facies contain
201 articulated bivalves and well-preserved, intact gastropods. Mean sand content ranges from
202 70% to 40%, with <10% clay found in all samples, and a varying proportion of shell
203 fragments, depending on the sedimentary facies. Four sedimentary facies were identified
204 within the CHS sediment cores: black sand facies, parallel and ripple cross laminated sand
205 facies, sandy shell hash facies, and a sandy silt facies (Figs. 4, 5). Grain-size distributions for
206 each sample aided in differentiating between the facies and in identifying subtle grain-size
207 trends. A total of 30 radiocarbon ages were obtained from 24 shells and six wood fragments
208 in the cores from the CHS (table 2). Ages range from modern to 12,195 cal. years B.P. Only
209 three ages in core HF-5 obtained from a 36-mg wood fragment (HF-5, 115 cm), a 20-mg

wood fragment (HF-5, 287 cm) and a gastropod shell are out of sequence. Core HF-1 has one out of sequence date, which was obtained from a 30-mg wood fragment.

***Black sand facies**:* The black sand facies appears in the lower portion of sediment cores HF-1, HF-7, and HF-4, as well as in the cutter nose of HF-3, which samples the seismic unit below the base of the CHS, package S_1 (Figs. 5, 6, 7). This facies is composed of clean fine-grained sand (average grain size 130 μm), with less than 5% silt and no clay. It has a unimodal grain-size and no skewness (Fig. 3). Shell fragments are scarce, comprising < 5% carbonate by weight. The namesake "black" color of this facies is due to the local Franciscan Complex sediment source area. Prominent rock types within the Franciscan Complex include sandstone, graywacke, conglomerate, greenstone, diabase, chert, serpentinite and glaucophane schist. Thus, sands sourced from it are rich in heavy minerals, including amphibole, pyroxene, epidote, sphene and magnetite. This mineral assemblage contrasts with the overlying brown shelf deposits, which have a lower portion of heavy minerals and higher proportion of shell fragments. In core HF-7, the black sand facies is comprised of two beds: a lower 20 cm-thick bed with parallel laminations and intact gastropods and an upper 13 cm-thick bed with no visible structures (Fig. 4a). The upper bed fines upward from fine to very fine sand (130 μm to 110 μm). The fauna identified in this facies includes the two species *Clathurella canfieldi* and *Truncatella californica*. Both of these species prefer a sandy habitat, among surf grass roots in the upper intertidal zone (Guz, 2007). Radiocarbon dates from gastropods within this facies yield ages between 12,195-9,524 cal. years B.P. (table 2).

Parallel- and ripple-cross laminated sand: This facies occurs in cores HF-1, HF-3 and HF-5, but is not found in nearby core HF-7 collected seaward of the CHS (Figs. 1, 5). This facies is composed of very fine sand (mean grain size 90 μm) with an average abundance of 50% sand, 40% silt, and 10% clay, as well as abundant shell fragments (~20% carbonate by weight). The grain size mode is 100 μm and the grain-size distribution is negatively skewed

(Fig. 3). The parallel and ripple cross laminated facies is composed of 10 - 20 cm-thick inversely graded (100 μm - 90 μm) to normally graded beds (90 μm to 60 μm). The inverse graded beds sit atop an erosive base; however, these are only preserved in cores HF-3 and HF-5. Within the inversely graded beds, faint ripple-cross laminations are observed, and whole gastropod shells are abundant, ranging in size from 0.5 to 2 cm (Fig. 4b). Within the fining upward sequences, there is a marked alternation of parallel laminations and ripple-cross laminations every ~5 cm. Commonly, this facies is capped by alternating very fine sand and silt laminae (Fig. 4c). The shell fragments, while present throughout the facies, are more concentrated at the base of the beds. The fauna present in this facies consists of two main species: *Callianax baetica* and *Amphissa versicolor. Callianax baetica* mainly inhabits sandy or muddy substrates in offshore areas in water depths of up to 65 m and is rarely found in intertidal areas (Sept, 2019). *Amphissa versicolor* is common to the upper sections of the sediment cores, within the parallel and ripple cross laminated sand facies. It only inhabits subtidal areas up to ~50 m depths and can adapt to many types of substrates (rocky or muddy) (Austin, 1985; Gotshall, 1994; Guz, 2007; Sept, 2019). Radiocarbon dates from gastropods and wood fragments within this facies yield ages ranging between ~7,500 – 900 cal years B.P. (table 2).

Sandy shell hash facies: This facies overlies the parallel and ripple cross laminated facies in cores HF-3 and HF-5, but is not present in cores HF-1 and HF-7 (Fig. 5). The sandy shell hash facies is composed of as many as five shell beds, almost entirely composed pebble sized shell fragments (ranging from 1 to 5 cm, on average 28-32% carbonate by weight) and fine to medium sand (300-500 μm). The individual shell hash beds are typically about 2 cm thick and are interbedded with ~ 2 cm thick beds of medium and fine parallel laminated sands (Fig. 4d). The matrix (non-shelly component) grain size is unimodal and has no skewness, with a mode at 330 μm (Fig. 3). The thickness and shell content of this facies decreases

basinward from 85 cm in core HF-5 (shell fragment content of 32% by mass) to 30 cm, in core HF-3 (shell fragment content of 24% by mass). Fauna in this facies is challenging to identify, as it is mainly composed of fragmented bivalve or gastropod shells. When intact gastropods are present, the most abundant species is Amphissa versicolor. Because of the lack of abundance of intact gastropods, only one radiocarbon date was obtained for this facies (from a *Amphissa versicolor* shell), yielding an age of 721-515 cal. years B.P. (table 2).

Sandy silt facies: The sandy silt facies comprises the top layer of all sediment cores (Fig. 5). The average grain size is 40 μm and it is composed of, on average, 65% silt, 30% sand, and 5% clay. The grain-size distribution is polymodal, with peaks at 100 μm, 50 μm and 30 μm (Fig. 3). No visible sedimentary structures other than burrowing were observed within the beds, and they contain fewer (~7% carbonate mass by weight) scattered shell fragments (0.2 mm) compared to the other facies found in the cores (Fig. 4e). Fauna in this facies is rarely present, but occasional *Amphissa versicolor* are identified. Radiocarbon dating from gastropod shells within this facies yield modern ages (table 2).

4.2 Seismic-reflection profiles

The chirp data across the CHS reveal the presence of three distinct seismic units: S_1, S_2, and S_3 (Figs. 6, 7). Seismic unit S_1 is the lowest of the identified units and is marked by weakly developed divergent, high amplitude, chaotic reflections with occasional reflection-free zones. This unit is found below and seaward of the CHS. Seismic unit S_2 overlies S_1, and is characterized by medium amplitude, basin dipping sigmoidal reflections. This unit pinches out at the bottomset of the CHS. Reflections in seismic unit S_2 are truncated against seismic unit S_3, which is distinguishable by its scoop shape and its high amplitude, subparallel reflections. This unit is not continuous through the clinoformal feature but rather develops as the fill of scour features scattered across the top of the CHS (Figs. 6, 7).

5. Facies Interpretation

The main body of the CHS, is composed of the parallel and ripple cross-laminated sand facies, which corresponds to seismic unit S_2. Seismic unit S_2 progrades over seismic unit S_1, which is comprised of the black sand facies, representing an older Younger Dryas stadial shoreface. Progradation of the CHS was promoted by a slowdown in the rate of RSL rise (Reynolds and Simms, 2015), an optimal condition for the formation of subaqueous prograding bodies, as sediment supply to the shelf area outpaces the rate of sea-level rise (Hernandez-Molina et al., 2000; Patruno et al., 2015; Patruno & Helland-Hansen, 2018; Budillon et al., 2022). Seismic unit S_3, which corresponds to the sandy shell hash facies, represents a younger erosive feature that has scoured and filled the clinoformal sediments with coarse grained (up to 5 cm) shell fragments and medium sands. The sandy silt facies most likely corresponds to the top of seismic unit S_2 and, where present, unit S_3. However, this contact is not discernable in the chirp data. Below we discuss each sedimentary facies and their role in building the subaqueous clinoform.

***Black sand facies**:* The oldest sediment observed in our cores is the black sand facies, which corresponds to seismic unit S_1. The seismic character, typical of shoreface deposits, and the well-sorted fine sand with parallel laminations and unimodal grain-size distribution of the black sand facies suggest deposition may have occurred within a lower to upper shoreface environment, where waves and currents are the principal mechanism of sediment transport (Niedoroda et al., 1984) and able to winnow the finer sediments, resulting in well sorted, parallel laminated sands (table 3). The *Clathurella canfieldi* and *Truncatella californica* gastropods that are only found within the black sand facies prefer an upper intertidal habitat in sandy bottoms, which suggest deposition in a shallower marine environment. Ages from this deposit correspond to the Younger Dryas interstadial (Table 2). During this time RSL in southern California is estimated to have been between -55 and -60 m (Reynolds and Simms,

2015; Yousefi et al., 2018). Considering cores HF-1 and HF-7 were collected in water depths of 82 and 81 m, respectively, we interpret the black sand facies as a unit deposited in much shallower water depths than present (less than 20 m) (Fig. 2). The post Younger Dryas ages obtained within this facies range from 10,035-9,524 cal. years B.P. (Table 2). The gastropods used for dating in this case were sampled from the top of the black sand facies, and were most likely subjected to post Younger Dryas reworking, such as draping, and bio-occupation.

The black sand facies is separated from the parallel and ripple cross laminated facies by a sharp erosive contact, and a < 2 cm thick bed of shell fragments (Fig. 5). This contact is always observed above the black sand facies, including cores HF-1, HF-4 and HF-7. Considering the missing time between the black sand facies and the parallel and ripple cross laminated facies, as well as the erosive nature of their contact, we interpret this contact as a wave ravinement surface (WRS). WRSs are commonly sculpted by waves during transgression and are often mantled by shell lag deposits (Cattaneo and Steel, 2003; Zecchin et al., 2019), much like the shell layer observed above the black sand facies. We propose that rapid sea-level rise post-dating the Younger Dryas stadial emplaced the shell lag deposit above the now relict shoreface deposit, represented by the black sand facies.

Parallel and ripple cross laminated sand facies*:* The parallel and ripple-cross laminated sand facies comprises seismic unit S_2, which pinches out at the foot of the CHS (Fig. 6). Based on the correlation between the cores and seismic profiles (Figs. 5, 6), the parallel and ripple cross laminated facies dominates the main prograding body of the CHS. Strata are organized in ~10 - 30 cm-thick beds, each of which displays an erosive base, overlain by inversely to normally graded beds that transition to a parallel and ripple cross laminated fining upward unit. Shell fragments are prevalent throughout the beds, amounting to 20 - 25% carbonate by weight, while wood material is rare. Siliciclastic sediment is thoroughly mixed with the shell fragments, indicating sediment mixing and minor amounts of

335 wood further support possible offshore transport by intrabasinal processes such as waves and
336 tides. Taken together, these beds are consistent with deposition by turbulent flows,
337 transitioning between upper- and lower-flow regimes, capable of producing parallel
338 laminations and grading into ripple cross lamination as a result of traction and fallout
339 processes (Sanders, 1960) (table 3). The slightly coarser grain sizes and inverse grading result
340 from dispersive pressures and a lag in transport of the coarser material (Hand, 1997). The
341 transition between the inverse graded and the normally graded sequences may represent the
342 'maximum' waxing of the flow (Mulder et al., 2003). As the flow loses velocity, a fining
343 upward unit is deposited, marked by an alternation of parallel laminations and ripple-cross
344 laminations. The top of the deposit fines upward to silty beds, which are often intercalated
345 with thin laminae of very fine sand. We interpret these silts as the fine-grained, late-stage
346 suspension deposits associated with some sort of sediment gravity flow.

347 Radiocarbon ages from the parallel and ripple cross laminated facies (seismic unit S_2)
348 suggest that deposition occurred between 7,088 – 6,749 cal. years B.P. (maximum age of
349 deposition; Table 2) and 1,157-898 cal. years B.P. During this time period, RSL along
350 California is estimated to be ~ 6.5 m bsl, and ~0.5 m bsl, respectively (Reynolds and Simms,
351 2015, Fig. 2) placing the CHS in water depths ranging between ~ 63.5 m and ~ 69.5 m at the
352 time of deposition (Fig. 2). Additionally, the fauna identified within the CHS further suggests
353 deposition in deeper water, as both *Callianax baetica* and *Amphissa versicolor* prefer a
354 subtidal habitat, in water depths of up to 65 m (Austin, 1985; Gotshall, 1994; Sept, 2019).

355 ***Sandy shell hash facies:*** The sandy shell hash facies is found in cores sampling
356 seismic unit S_3. Seismic unit S_3 has an irregular erosional base that appears to represent
357 scour into the underlying sediment of seismic unit S_2. Unit S_3 , comprised of the sandy shell
358 hash facies, is not laterally continuous through the CHS, but rather organized in localized
359 'pockets' (Figs. 6, 7). The basinward extent of this unit is less than that of the parallel and

ripple cross laminated sand facies, pinching out between core HF-3 and HF-1 (Fig. 5). This facies is coarser and richer in biogenic material (medium sand and shell fragments up to 5 cm) than the parallel and ripple cross laminated facies. Based on the unimodal, coarsely skewed grain size distribution (GSD) of the sandy shell hash facies and the presence of large shell fragments and parallel laminations, we invoke strong wave action as responsible for the suspension, reworking, and seaward advection of the sediment, where the coarser material is eventually separated from its finer particles, leaving behind a coarsely skewed, shelly deposit (Table 3) (Hernandez-Molina et al., 2000; Zecchin et al., 2019). The sandy shell hash facies is most likely not genetically linked to the flow deposits, but rather represents a younger storm deposit that scoured into the clinoformal sediment.

***Sandy silt facies**:* The sandy silt facies, which blankets the CHS, is most likely not genetically linked to the flows feeding the progradation of the CHS. This sedimentary facies is not visible in the seismic data and cannot be grouped into one seismic package. However, the sandy silt facies is found in cores throughout the CHS (topset, foreset, bottomset) and it maintains a near uniform thickness, and does not pinch out in deeper water depths as does the parallel and ripple cross laminated facies (Fig. 5). It post-dates ~700 years B.P. and is thus interpreted to represent modern day hemipelagic accumulation and is similar to sediment at the top of some of the fining-upward sequences in the underlying parallel and ripple cross laminated facies.

6. Discussion

6.1 Genesis and evolution of the Cross Hosgri Slope

In chirp profiles the CHS resembles the infralittoral prograding wedges (IPW) of Hernandez-Molina et al. (2000) recently reviewed by Budillon et al. (2022), displaying thin topsets with high acoustic reflectivity and foresets with seaward dipping, high amplitude reflections. They describe IPWs as depositional bodies defined by internal clinoforms and

385 whose main mechanism of progradation is dictated by storm waves. Here we explore the
386 driving mechanisms of progradation for the CHS and, by analogy, other IPWs.

387 Given the absence of a fluvial source other than the relatively small (123 km^2) Santa
388 Rosa watershed located about 10 km north of the CHS, fluvial-deltaic sediment transport is
389 likely not a viable mechanism for driving CHS progradation. However, the central California
390 shelf is characterized by a high energy wave climate, specifically in the winter months, when
391 wave activity associated with storms is greatest (Dingler et al., 1982; Storlazzi and Griggs,
392 2000; Storlazzi and Wingfield, 2005). We propose that intense wave action entrained and
393 mobilized sandy and silty shelf sediment and shell fragments, which were swept to the
394 seaward edge of the topset of the CHS where that sediment fed WSGFs that prograded the
395 CHS. A break in slope given by the relict shoreface beneath the CHS (seismic unit S1, black
396 sand facies) allowed for a nucleation point to build the initial clinoform geometry of the CHS.

397 To explore the possible role of WSGFs in the growth of the CHS, we examine the two
398 dominant factors that contribute to these flows: the slope of the seafloor, and wave influence.
399 Wright et al. (2001) showed that gravity currents can only be sustained at a minimum slope,
400 defined by:

401 $$\sin\theta = (C_d / Ri_{cr}) (|u| / u_g) \qquad (1)$$

402 where C_d is the bottom drag coefficient, Ri_{cr} is the critical Richardson number, $|u|$ represents
403 the velocity scale related to friction on the gravity current, and u_g is the speed of the gravity
404 current. While Ri numbers as small as 0.01 have been suggested for sandy environments as
405 in the case of predominantly medium sands of Flores et al. (2018), we use the widely
406 accepted $Ri_{cr} = 0.25$ and $C_d \sim 0.003$ usually applied to finer sediments (silt and clay) (Scully
407 et al., 2003; Wright et al., 2001), as the sediment comprising the prograding portion of the
408 CHS is on average 50% very fine sand, 40% silt, and 10% clay. In a scenario with no wave
409 influence, $|u|$ equals u_g in equation (1), and the minimum slope to sustain gravity currents

410 corresponds to 0.7° (Wright and Friedrichs, 2006; Wright et al., 2001). The slope of the beds
411 below the CHS (seismic unit S_1, Fig. 6) is 1.3°, suggesting sustained movement of a wave-
412 supported gravity flow is possible at the location of the CHS. However, the shelf slope
413 seaward and landward of the CHS varies between 0.4° - 0.6 ° (Johnson et al., 2014), a value
414 below the minimum threshold for downslope gravity movement.

415 Wave influence along the wave-dominated California shelf must, however, be taken
416 into account when using equation (1). In this scenario, $|u| > u_g$ in equation (1), suggesting that
417 sediment suspension increases, promoting sediment flows at shelf slopes shallower than 0.7°
418 (Wright et al., 2001). We explore this possibility by using average wave period and
419 significant wave height to estimate the necessary conditions of orbital wave velocities to
420 entrain sediments at depth. By calculating the maximum orbital velocity obtained by swell
421 waves, Porter-Smith et al. (2004) showed that when near bed currents accelerate from zero to
422 a maximum value, they may exceed the threshold value where a specific grain size can be
423 mobilized. Using Porter-Smith et al. (2004):

424 $$U_{max} = (\pi H) / [T \sinh(2 \pi h / \lambda)] \qquad (2)$$

425 where H represents the wave height, h is the water depth, and λ is the wavelength (Porter-
426 Smith et al., 2004). The critical threshold for grain movement suggested by Clifton and
427 Dingler (1984) is:

428 $$U_{cr} = 33.3(TD)^{0.33} \qquad (3)$$

429

430 where T is the wave period, and D is the grain diameter. If the maximum velocity of the
431 waves (U_{max}) exceeds the threshold speed (U_{cr}), then mobilizing sediment with a grain
432 diameter of D will be possible (Porter-Smith et al., 2004). We solve for U_{max} under both
433 winter and summer conditions in central California, using data from the National Data Buoy
434 Center of the NOAA.gov database (station ID: 46028, fig. 1b) for the years between 1983-

435 2010. At this time, constraints on paleo-wave conditions for the Holocene along central
436 California are limited. As climatic conditions have not significantly changed in the last 7 ka
437 in central California (Dupre, 1983, Kirby et al., 2005), this allows for present day wave
438 statistics to be used in this study. We find that under winter swell conditions, U_{max} exceeds
439 U_{cr} for a grain diameter of 90 μm (mean grain size in the parallel and ripple cross laminated
440 facies) in 10% of the cases at a depth of 70 m (Figs. 8, 9). However, these conditions for
441 sediment remobilization are obtained less often at 85 m depth, where remobilization occurs in
442 < 2% of the cases (Figs. 8, 9). These observations suggest remobilization of the sediment is
443 possible under winter swell conditions at the topset of the CHS (70 m water depth), while it is
444 less likely to occur basinward of the foot of the CHS (~85 m water depth). In the case of
445 summer swell conditions, U_{max} rarely exceeds U_{cr} (ensuing only 0.2% of the times, at the
446 topset of the CHS, and 0.001% of the times at the foot of the CHS; Figs. 8, 9), suggesting
447 remobilization of the sediment by swell waves is not common under fair-weather conditions.
448 While we recognize that U_{max} could be affected by currents in the area, we treat wave action
449 as the main contributor to U_{max}, as the two largest currents in this region, the California
450 Current and the Davidson Current do not appear capable of entraining sediment of the size
451 comprising the CHS. The California Current flows at the shelf edge and extends up to 200
452 km from the coast. Even at the surface, where it maintains its highest speeds, its velocity of
453 0.05 m/s is too low to remobilize sediments of the size comprising the CHS (Auad et al.,
454 2011) (Eq. 2, 3). The Davidson Current, while closer to shore, is weaker than the California
455 Current, and flows northward (Checkley and Barth, 2009; Reid and Schwartzlose, 1962), the
456 opposite direction of the south-west progradation of the CHS. We suggest the progradation
457 of the CHS is promoted by intense winter storm waves, which are capable of moving very
458 fine sand grains at water depths up to ~70 m. An increase in shelf gradient (from 0.4° to 1.3°)
459 given by a relict shoreface (black sand facies) acts as a nucleation point for clinoform

460 progradation. Here WSGFs are initiated, which travel over the rollover point, and
461 consequently cascade over the foreset promoting clinoform progradation. Without sustained
462 waves and a low shelf gradient at the bottom set (0.4°) they cannot travel beyond the toe of
463 the foreset. During fair weather conditions, fine silts and clays of the sandy silt facies settle
464 out onto the seafloor. We suggest the sandy silt facies only accumulates in between large
465 storms, and once WSGFs are triggered by extreme events, these finer sediments are eroded
466 and/or reworked into the flows.

467 Progradation of the CHS seems to have stopped, or paused around 0.7 ka. We are not
468 certain as to why deposition stopped, as conditions appear to be favorable for their
469 development given today's wave climate. One possibility for the break in WSGF activation
470 may be a large storm event(s) that simultaneously emplaced the sandy shell hash facies
471 (forming scours in the CHS) and removed all fine materials from the source area. As a result,
472 triggering of WSGFs may have been interrupted as a result of a limited supply of fine
473 sediment that has yet to recover from the event.

474 The environmental setting of the CHS can be used as a guideline for establishing the
475 conditions necessary for the formation of subaqueous clinoforms built by WSGFs.
476 Clinoformal sediment accumulation require high enough wave energy to suspend sand at the
477 seafloor. In the case of the CHS in ~70 m water depth, significant wave heights need to
478 exceed ~ 4 m with wave periods of ~10 seconds to mobilize very fine sand. While waves are
479 a crucial component to initializing WSGFs, a steep enough shelf gradient is required to
480 promote sustained gravity flows. Any steep gradient shelf (> 0.7°) with a high energy wave
481 climate is considered to be an ideal framework to produce WSGFs. Alternatively, on gentler
482 shelves, a zone of high relief on the seafloor (produced by tectonic activity, or a
483 paleoshoreline) can also act as a nucleation point for clinoform growth by WSGFs. Thus, it is
484 likely that subaqueous clinoforms built by WSGFs can occur along any shelf, even sediment

starved areas such as the shelf north of Estero Bay, pending the right wave regime and shelf gradient. Shelf subaqueous clinoforms, specifically when formed by WSGFs in the absence of direct fluvial input, demonstrate that continental shelves are dynamic environments rather than a zone of bypass, and that it is possible for sediment accumulation to occur even during a sea-level highstand.

One intriguing hypothesis concerning the gravity flows comprising the CHS involves tectonic activity. The CHS is cut by the Hosgri fault, an active Holocene structure with a proposed slip rate of 2±0.9 mm/yr (Johnson et al., 2014). Sediment gravity flows can be triggered by earthquakes (e.g., along the Cascadia Subduction Zone) (Goldfinger et al., 2003) thus, each of the turbulent sediment flow units may represent a significant ground-shaking event. However, following a seismic triggered sediment failure a scar on the seafloor should be visible, and none is visualized in the bathymetry data from Johnson et al. (2014). Furthermore, without an independent record of earthquakes on the Hosgri fault it is not possible to test this hypothesis at the current time.

6.2 Similar shelf features

Several bathymetric features along the central California shelf have been mapped and described as prograding latest Pleistocene and Holocene sediment bars (Johnson et al., 2019), only some of which are adjacent to the mouths of significant coastal watersheds. These features have similar orientations and scales as the CHS, and occur at water depths ~ 50 m. Given these observations, WSGF-built subaqueous clinoforms are likely more widespread along the central California shelf. Similar features, such as IPWs, have been mapped across the Italian peninsula and other places in the Mediterranean (Budillon et al., 2022; Hernandez-Molina et al., 2000), but few have been cored or sampled.

6.3 A facies model for sandy wave-supported gravity flows and associated subaqueous clinoforms

510 Our analysis of the sedimentary facies near the CHS allows us to propose a facies
511 model for a subaqueous clinoform, or an IPW, composed of sandy WSGF deposits (Fig. 10).
512 The parallel and ripple cross laminated facies is deposited by the WSGF building the
513 subaqueous clinoform. The WSGF deposits are characterized by an erosive base indicating
514 emplacement by a turbulent flow. Above the erosive base, is an inversely graded bed with
515 abundant shell fragments and fine to medium sands from the most energetic parts of the flow,
516 where bedload is deposited as inverse grading as a result of the lag in transport of the coarser
517 material (Hand, 1997). As the peak of the flow passes, the energy decreases as the turbulent
518 flow oscillates between upper- and lower-flow regimes, producing alternating parallel and
519 ripple cross laminated beds of very fine sands. The transition between reverse and normal
520 grading as well as the alternation between parallel and ripple cross laminations indicates a
521 waxing and waning of the flow. The alternations in the flow are most likely due to temporal
522 changes in wave intensity. Finally, an increase in the fallout rate as the flow begins to
523 dissipate causes deposition of the suspended load, emplacing a silt cap at the top of the beds
524 (Fig. 10). These deposits are similar to the 'wave modified turbidites' sourced by
525 hyperpycnal flows as described by Lamb et al., (2008). However, in our scenario the gravity
526 flow is triggered by wave action itself rather than following a river flood, and later sustained
527 by an increase in the shelf slope.

528 **7. Conclusions**

529 Chirp data, sediment cores, and radiocarbon ages are used to describe the age and origin
530 of a wave-supported gravity flow (WSGF)-built subaqueous clinoform – or Infralittoral
531 Prograding Wedges (IPW), sensu Hernandez-Molina et al., (2000) – along the central
532 California shelf locally known as the Cross Hosgri Slope (CHS). In the absence of sediment
533 cores, the CHS had previously been interpreted to be a drowned shoreface paired to a now
534 eroded sandspit (Johnson et al., 2014). While the presence of a drowned shoreface is also

identified in this study, we find that a subaqueous clinoform nucleated atop the relict shoreface. Its mode of progradation was set up by winter swell waves remobilizing shelf sediment and sweeping them across the seafloor until they reached a break in slope, provided by the relict shoreface, where the finer sediments transitioned into sediment gravity flows leaving behind several fining upward beds marked by sedimentary structures indicative of pulsating flows. We suggest that WSGFs can form in sandy environments and do not necessarily need to be triggered by or sourced from river floods. We propose a facies model for sandy WSGF deposits, characterized by an erosive base, a sandy coarsening upward bed, followed by very fine sands marked by parallel and ripple cross lamination, and capped by interbedded very fine sands and silts (Fig. 10). Furthermore, this study provides a model for the formation of subaqueous clinoforms that occur in isolation and whose feeding mechanism mainly relies on winter swell. Their proper identification as subaqueous sandy bodies is important as to distinguish them from low stand deposits (Patruno et al., 2015; Peng et al., 2020).

8. Data Availability

Datasets related to this article can be found at https://doi.org/10.5066/P9A0U8J7, an open-source online data repository hosted by the USGS (Snyder et al., 2022).

Acknowledgements

This work was funded through a gift from Pacific Gas and Electric (PG&E), as well as a grant from the U.S. Geological Survey (USGS) National Earthquake Hazard Reduction Program (NEHRP) grant number G20AS00042 to University of California Santa Barbara. We also thank the captain and crew of the M/V *Bold Horizon*, John Southon and Chanda Bertrand at University of California Irvine for their help with radiocarbon dating, as well as

559 Vanessa Delnavaz at Santa Barbara Museum of Natural History for her help with shell
560 identification. Any use of trade, product, or firm names is for descriptive purposes only and
561 does not imply endorsement by the U.S. Government.

562
563 **Bibliography**

564 Auad, G., Roemmich, D., Gilson, J., 2011. The California Current System in relation to the
565 Northeast Pacific Ocean circulation. Progress in Oceanography 91, 576–592.
566 https://doi.org/10.1016/j.pocean.2011.09.004

567 Austin, W.C., 1985. An Annotated Checklist of Marine Invertebrates in the Cold Temperate
568 Northeast Pacific. Khoyatan Marine Laboratory.

569 Bakker, E., Slack, G., 1985. An Island Called California: An Ecological Introduction to Its
570 Natural Communities, Revised and Expanded, 2nd ed. Univ of California press.

571 Bray, N.A., Keyes, A., Morawitz, W.M.L., 1999. The California Current system in the
572 Southern California Bight and the Santa Barbara channel. Journal of Geophysical
573 Research-Oceans 104, 7695–7714. https://doi.org/Doi 10.1029/1998jc900038

574 Budillon, F., Amodio, S., Alberico, I., Contestabile, P., Vacchi, M., Innangi, S., Molisso, F.,
575 2022. Present-day infralittoral prograding wedges (IPWs) in Central-Eastern Tyrrhenian
576 Sea: Critical issues and challenges to their use as geomorphological indicators of sea
577 level. Marine Geology. https://doi.org/10.1016/j.margeo.2022.106821

578 California State University Monterey Bay Sea Floor Mapping Lab (CSUMB) (2012).
579 Seafloor Mapping Lab at CSUMG, http://seafloor.csumb.edu/SFMLwebDATA_c.htm

580 Cattaneo, A., Steel, R.J., 2003. Transgressive deposits: a review of their variability. Earth-
581 Science Reviews 62, 187–228. https://doi.org/10.1016/S0012-8252(02)00134-4

582 Checkley, D.M., Barth, J.A., 2009. Patterns and processes in the California Current System.
583 Progress in Oceanography 83, 49–64. https://doi.org/10.1016/j.pocean.2009.07.028

584 Chelton, D.B., 1984. Seasonal variability of alongshore geostrophic velocity off central
585 California. Journal of Geophysical Research 89, 3473.
586 https://doi.org/10.1029/JC089iC03p03473

587 Clark, J.A., Farrell, W.E., Peltier, W.R., 1978. Global Changes in Post-Glacial Sea-Level -
588 Numerical-Calculation. Quaternary Research 9, 265–287. https://doi.org/Doi
589 10.1016/0033-5894(78)90033-9

590 Clifton, H., Dingler, J., 1984. Wave-formed structures and paleoenvironmental
591 reconstruction. https://doi.org/10.1016/0025-3227(84)90149-X

592 Collins, C.A., Pennington, J.T., Castro, C.G., Rago, T.A., Chavez, F.P., 2003. The California
593 Current system off Monterey, California: physical and biological coupling. Deep-Sea
594 Research Part Ii-Topical Studies in Oceanography 50, 2389–2404.
595 https://doi.org/10.1016/S0967-0645(03)00134-6

Dickinson, W.R., Ducea, M., Rosenberg, L.I., Greene, H.G., Graham, S.A., Clark, J.C., Weber, G.E., Kidder, S., Ernst, W.G., Brabb, E.E., 2005. Net Dextral Slip, Neogene San Gregorio-Hosgri Fault Zone, Coastal California: Geologic Evidence and Tectonic Implications, Net Dextral Slip, Neogene San Gregorio-Hosgri Fault Zone, Coastal California: Geologic Evidence and Tectonic Implications. Geological Society of America. https://doi.org/10.1130/spe391

Dingler, J.R., Anima, R.J., Molzan, D.E., Luepke, G., Peterson, C.L., 1982. A field study of littoral processes in Estero Bay, California, Open-File Report. U.S. Geological Survey.

Dupré, W.R., 1984. Reconstruction of paleo-wave conditions during the late Pleistocene from marine terrace deposits, Monterey bay, California. Developments in Sedimentology 39, 435-454. https://doi.org/10.1016/S0070-4571(08)70158-4

Fernández-Salas, L.M., Dabrio, C.J., Goy, J.L., Díaz del Río, V., Zazo, C., Lobo, F.J., Sanz, J.L., Lario, J., 2009. Land–sea correlation between Late Holocene coastal and infralittoral deposits in the SE Iberian Peninsula (Western Mediterranean). Geomorphology 104, 4–11. https://doi.org/10.1016/j.geomorph.2008.05.013

Flores, R.P., Rijnsburger, S., Meirelles, S., Horner-Devine, A.R., Souza, A.J., Pietrzak, J.D., Henriquez, M., Reniers, A., 2018. Wave Generation of Gravity-Driven Sediment Flows on a Predominantly Sandy Seabed. Geophysical Research Letters 45, 7634–7645. https://doi.org/10.1029/2018GL077936

Goldfinger, C., Nelson, C.H., Johnson, J.E., 2003. Holocene earthquake records from the Cascadia subduction zone and northern San Andreas fault based on precise dating of offshore turbidites. Annual Review of Earth and Planetary Sciences 31, 555–577. https://doi.org/10.1146/annurev.earth.31.100901.141246

Gotshall, D., 1994. Guide to marine invertebrates: Alaska to Baja California. Sea Challengers, Monterey, California.

Guz, S.S., 2007. The light and smith manual: Intertidal invertebrates from central California to Oregon. Library Journal 132, 154.

Hand, B.M., 1997. Inverse grading resulting from coarse-sediment transport lag. Journal of Sedimentary Research 67, 124–129. https://doi.org/10.1306/D426850E-2B26-11D7-8648000102C1865D

Hanson, K.L., Lettis, W.R., McLaren, M., Savage, W., Hall, T.N., 1995. Style and Rate of Quaternary Deformation of the Hosgri Fault Zone, Offshore South-Central Coastal California.

Hartwell, S. R., D. P. Finlayson, P. Dartnell, and S. Y. Johnson (2013). Bathymetry and acoustic backscatter, Estero Bay, California, U.S. Geol. Surv. Open-File Rept. 2013-1225, http://pubs.usgs.gov/of/2013/1225/abstract.html

Hawley, R., Diggory, Z., Wald, S., 2012. Santa Rosa Creek watershed manegement plan. Prepared for the California Department of fish and game. California Department of fish and game 169.

635 Heaton, T.J., Köhler, P., Butzin, M., Bard, E., Reimer, R.W., Austin, W.E.N., Ramsey, C.B.,
636 Grootes, P.M., Hughen, K.A., Kromer, B., Reimer, P.J., Adkins, J., Burke, A., Cook,
637 M.S., Olsen, J., Skinner, L.C., 2020. Marine20—The Marine Radiocarbon Age
638 Calibration Curve (0–55,000 cal BP). Radiocarbon 62, 779–820.
639 https://doi.org/10.1017/RDC.2020.68

640 Hernandez-Molina, F.J., Fernandez-Salas, L.M., Lobo, F., Somoza, L., Diaz-del-Rio, V.,
641 Alveirinho Dias, J.M., 2000. The infralittoral prograding wedge: a new large-scale
642 progradational sedimentary body in shallow marine environments. Geo-Marine Letters
643 20, 109–117. https://doi.org/10.1007/s003670000040

644 Hickey, B.M., 1998. Coastal oceanography of western North America, from the tip of Baja
645 California to Vancouver Island. The Sea 11, 345–393, 1062.

646 Johnson, S.Y., Hartwell, S.R., Dartnell, P., 2014. Offset of Latest Pleistocene Shoreface
647 Reveals Slip Rate on the Hosgri Strike-Slip Fault, Offshore Central California. Bulletin
648 of the Seismological Society of America 104, 1650–1662.
649 https://doi.org/10.1785/0120130257

650 Johnson, S.Y., Hartwell, S.R., Watt, J.T., Beeson, J.W., Dartnell, P., 2019. Offshore shallow
651 structure and sediment distribution, Point Sur to Point Arguello, central California: U.S.
652 Geological Survey Open-File Report 2018–1158, 3 sheets, scales 1:150,000 and
653 1:200,000. https://doi.org/https://doi.org/10.3133/ofr20181158.

654 Johnson, S.Y., Watt, J., 2012. Influence of fault trend, bends, and convergence on shallow
655 structure and geomorphology of the Hosgri strike-slip fault, offshore central California.
656 Geosphere. https://doi.org/10.1130/GES00830.1

657 Johnson, S.Y., Watt, J.T., Hartwell, S.R., Kluesner, J.W., 2018. Neotectonics of the Big Sur
658 Bend, San Gregorio-Hosgri Fault System, Central California. Tectonics 37, 1930–1954.
659 https://doi.org/10.1029/2017TC004724

660 Kämpf, J., Chapman, P., 2016. The California Current Upwelling System, in: Upwelling
661 Systems of the World. Springer International Publishing, Cham, pp. 97–160.

662 Kirby, M. E., Lund, S. P. and Poulsen, C. J. 2005. Hydrologic variability and the onset of
663 modern El Nin˜o–Southern Oscillation: a 19 250-year record from Lake Elsinore,
664 southern California. J. Quaternary Sci., Vol. 20 pp. 239–254. ISSN 0267-8179.

665 Lamb, M.P., Myrow, P.M., Lukens, C., Houck, K., Strauss, J., 2008. Deposits from Wave-
666 Influenced Turbidity Currents: Pennsylvanian Minturn Formation, Colorado, U.S.A.
667 Journal of Sedimentary Research 78, 480–498. https://doi.org/10.2110/jsr.2008.052

668 Langenheim, V.E., Jachens, R.C., Graymer, R.W., Colgan, J.P., Wentworth, C.M., Stanley,
669 R.G., 2013. Fault geometry and cumulative offsets in the central Coast Ranges,
670 California: Evidence for northward increasing slip along the San Gregorio–San Simeon–
671 Hosgri fault. Lithosphere 5, 29–48. https://doi.org/10.1130/L233.1

672 Ma, Y., Wright, L.D., Friedrichs, C.T., 2008. Observations of sediment transport on the
673 continental shelf off the mouth of the Waiapu River, New Zealand: Evidence for
674 current-supported gravity flows. Continental Shelf Research 28, 516–532.
675 https://doi.org/10.1016/J.CSR.2007.11.001

Martínez-Carreño, N., García-Gil, S., Cartelle, V., 2017. An unusual Holocene fan-shaped subaqueous prograding body at the back of the Cíes Islands ridge (Ría de Vigo, NW Spain): Geomorphology, facies and stratigraphic architecture. Marine Geology 385, 13–26. https://doi.org/10.1016/J.MARGEO.2016.11.015

Mitchell, N.C., 2012. Modeling The Rollovers of Sandy Clinoforms from the Gravity Effect On Wave-Agitated Sand. Journal of Sedimentary Research 82, 464–468.

Mulder, T., Syvitski, J.P.M., Migeon, S., Faugères, J., Savoye, B., 2003. Marine hyperpycnal flows: initiation, behavior and related deposits. A review. Marine and Petroleum Geology 20, 861–882. https://doi.org/10.1016/j.marpetgeo.2003.01.003

Niedoroda, A.W., Swift, D.J.P., Hopkins, T.S., Ma, C.-M., 1984. Shoreface Morphodynamics on Wave-Dominated Coasts, in: Greenwood, B., Davis, R.A. (Eds.), Developments in Sedimentology. Elsevier, pp. 331–354.

Nishenko, S., G. H, H., Hogan, P., Bergkamp, B., 2018. Geometry and Late Pleistocene Displacement of the Shoreline and Oceano Fault Zones, San Luis Obispo Bay, California. Bulletin of the Seismological Society of America. https://doi.org/10.1785/0120160177

Ogston, A.S., Cacchione, D.A., Sternberg, R.W., Kineke, G.C., 2000. Observations of storm and river flood-driven sediment transport on the northern California continental shelf. Continental Shelf Research 20, 22. https://doi.org/10.1016/S0278-4343(00)00065-0

Ozdemir, C.E., 2016. Turbulence-resolving, two-phase flow simulations of wave-supported gravity flows: A conceptual study. Journal of Geophysical Research: Oceans 121, 8849–8871. https://doi.org/10.1002/2016jc012061

Patruno, S., Hampson, G.J., Jackson, C., 2015. Quantitative characterisation of deltaic and subaqueous clinoforms. Earth-Science Reviews 142, 79–119.

Patruno, S., Helland-Hansen, W., 2018. Clinoforms and clinoform systems: Review and dynamic classification scheme for shorelines, subaqueous deltas, shelf edges and continental margins. Earth-Science Reviews 185, 202–233.

Peng, Y., Olariu, C., Steel, R.J., 2020. Recognizing tide- and wave-dominated compound deltaic clinothems in the rock record. Geology 48, 1149–1153.

Pirmez, C., Pratson, L.F., Steckler, M.S., 1998. Clinoform development by advection-diffusion of suspended sediment: Modeling and comparison to natural systems. Journal of Geophysical Research: Solid Earth 103, 24141–24157. https://doi.org/10.1029/98JB01516

Porter-Smith, R., Harris, P.T., Andersen, O.B., Coleman, R., Greenslade, D., Jenkins, C.J., 2004. Classification of the Australian continental shelf based on predicted sediment threshold exceedance from tidal currents and swell waves. Marine Geology 211, 1–20. https://doi.org/10.1016/j.margeo.2004.05.031

Puig, P., Ogston, A.S., Mullenbach, B., Nittrouer, C., Sternberg, R., 2003. Shelf-to-Canyon sediment-transport processes on the Eel Continental Margin (Northern California).

715 Marine Geology - MAR GEOLOGY 193, 129–149. https://doi.org/10.1016/S0025-
716 3227(02)00641-2

717 Ramirez, A.R., de Guzman, M.E., Dawson, T.E., Ackerly, D.D., 2020. Plant hydraulic traits
718 reveal islands as refugia from worsening drought. Conservation Physiology 8.
719 https://doi.org/10.1093/conphys/coz115

720 Ramsdell, R.C., Miedema, S.A., Talmon, A.M., Asme, Asme, O.O., Arctic Engn, D., 2011.
721 HYDRAULIC TRANSPORT OF SAND/SHELL MIXTURES, in: 30th International
722 Conference on Ocean, Offshore and Arctic Engineering. Rotterdam, NETHERLANDS,
723 pp. 533-+.

724 Reid, J.L., Schwartzlose, R.A., 1962. Direct measurements of the Davidson Current off
725 central California. Journal of Geophysical Research 67, 2491–2497.
726 https://doi.org/10.1029/jz067i006p02491

727 Reimer, P.J., Austin, W.E.N., Bard, E., Bayliss, A., Blackwell, P.G., Ramsey, C.B., Butzin,
728 M., Cheng, H., Edwards, R.L., Friedrich, M., Grootes, P.M., Guilderson, T.P., Hajdas,
729 I., Heaton, T.J., Hogg, A.G., Hughen, K.A., Kromer, B., Manning, S.W., Muscheler, R.,
730 Palmer, J.G., Pearson, C., Plicht, J. van der, Reimer, R.W., Richards, D.A., Scott, E.M.,
731 Southon, J.R., Turney, C.S.M., Wacker, L., Adolphi, F., Büntgen, U., Capano, M.,
732 Fahrni, S.M., Fogtmann-Schulz, A., Friedrich, R., Köhler, P., Kudsk, S., Miyake, F.,
733 Olsen, J., Reinig, F., Sakamoto, M., Sookdeo, A., Talamo, S., 2020. The IntCal20
734 Northern Hemisphere Radiocarbon Age Calibration Curve (0–55 cal kBP). Radiocarbon
735 62, 725–757. https://doi.org/10.1017/RDC.2020.41

736 Reynolds, L.C., Simms, A.R., 2015. Late Quaternary relative sea level in Southern California
737 and Monterey Bay. Quaternary Science Reviews 126, 57–66.
738 https://doi.org/10.1016/j.quascirev.2015.08.003

739 Sanders, J.E., 1960. Primary Sedimentary Structures Formed by Turbidity Currents and
740 Related Resedimentation Mechanisms.

741 Schattner, U., Lobo, FJ., Lopez-Quiros, A., Nascimento, JLD, de Mahiques, M.M., 2020.
742 What feeds shelf-edge clinoforms over margins deprives of adjacent land sources? An
743 example from southeastern Brazil. Basin research 32, 293-301.
744 https://doi.org/10.1111/bre.12397

745 Scully, M.E., Friedrichs, C.T., Wright, L.D., 2003. Numerical modeling of gravity-driven
746 sediment transport and deposition on an energetic continental shelf: Eel River, northern
747 California. Journal of Geophysical Research: Oceans 108, 3120.
748 https://doi.org/10.1029/2002JC001467

749 Sept, J.D., 2019. The New Beachcomber's Guide to the Pacific Northwest. Harbour
750 Publishing.

751 Sequeiros, O.E., Naruse, H., Endo, N., Garcia, M.H., Parker, G., 2009. Experimental study on
752 self-accelerating turbidity currents. Journal of Geophysical Research 114, C05025.
753 https://doi.org/10.1029/2008JC005149

754 Snyder, G.R., Balster-Gee, A.F., Kluesner, J.W., Johnson, S.Y., Medri, E., Simms R., A.,
755 Nishenko, S., Greene, G., Conrad, J.E., 2022. Geophysical and core sample data

collected offshore central California, during field activity 2019-651-FA. https://doi.org/https://doi.org/10.5066/P9A0U8J7

Sperazza, M., Moore, J.N., Hendrix, M.S., 2004. High-Resolution Particle Size Analysis of Naturally Occurring Very Fine-Grained Sediment Through Laser Diffractometry. Journal of Sedimentary Research 74, 736–743. https://doi.org/10.1306/031104740736

Stanford, J.D., Hemingway, R., Rohling, E.J., Challenor, P.G., Medina-Elizalde, M., Lester, A.J., 2011. Sea-level probability for the last deglaciation: A statistical analysis of far-field records. Global and Planetary Change 79, 193–203. https://doi.org/10.1016/j.gloplacha.2010.11.002

Steel, R., Olsen, T., 2002. Clinoforms, Clinoform Trajectories and Deepwater Sands, in: Sequence Stratigraphic Models for Exploration and Production: Evolving Methodology, Emerging Models, and Application Histories: 22nd Annual. SOCIETY OF ECONOMIC PALEONTOLOGISTS AND MINERALOGISTS, pp. 367–380. https://doi.org/10.5724/gcs.02.22.0367

Storlazzi, C.D., Griggs, G.B., 2000. Influence of El Nino-Southern Oscillation (ENSO) events on the evolution of central California's shoreline. Geological Society of America Bulletin 112, 236–249. https://doi.org/10.1130/0016-7606(2000)112<236:IOENOE>2.0.CO;2

Storlazzi, C.D., Wingfield, D.K., 2005. Spatial and Temporal Variations in Oceanographic and Meteorologic Forcing Along the Central California Coast, 1980-2002. U.S. Geological Survey.

Stuiver, M., Reimer, P.J., Reimer, R.W., 2022. CALIB 14C Calibration Program.

Traykovski, P., Wiberg, P.L., Geyer, W.R., 2007. Observations and modeling of wave-supported sediment gravity flows on the Po prodelta and comparison to prior observations from the Eel shelf. Continental Shelf Research 27, 375–399. https://doi.org/10.1016/j.csr.2005.07.008

Vericat, D., Batalla, R.J., Garcia, C., 2006. Breakup and reestablishment of the armour layer in a large gravel-bed river below dams: The lower Ebro. Geomorphology 76, 122–136. https://doi.org/10.1016/j.geomorph.2005.10.005

Wright, L.D., Friedrichs, C.T., 2006. Gravity-driven sediment transport on continental shelves: A status report. Continental Shelf Research 26, 2092–2107. https://doi.org/10.1016/J.CSR.2006.07.008

Wright, L.D., Friedrichs, C.T., Kim, S.C., Scully, M.E., 2001. Effects of ambient currents and waves on gravity-driven sediment transport on continental shelves. Marine Geology 175, 25–45. https://doi.org/10.1016/S0025-3227(01)00140-2

Yousefi, M., Milne, G.A., Love, R., Tarasov, L., 2018. Glacial isostatic adjustment along the Pacific coast of central North America. Quaternary Science Reviews 193, 288–311. https://doi.org/10.1016/j.quascirev.2018.06.017

794 Yue, L., Cheng, Z., Hsu, T., 2020. A Turbulence-Resolving Numerical Investigation of
795 Wave-Supported Gravity Flows. Journal of Geophysical Research: Oceans 125.
796 https://doi.org/10.1029/2019JC015220

797 Zecchin, M., Catuneanu, O., Caffau, M., 2019. Wave-ravinement surfaces: Classification and
798 key characteristics. Earth-Science Reviews 188, 210–239.
799 https://doi.org/10.1016/j.earscirev.2018.11.011

800

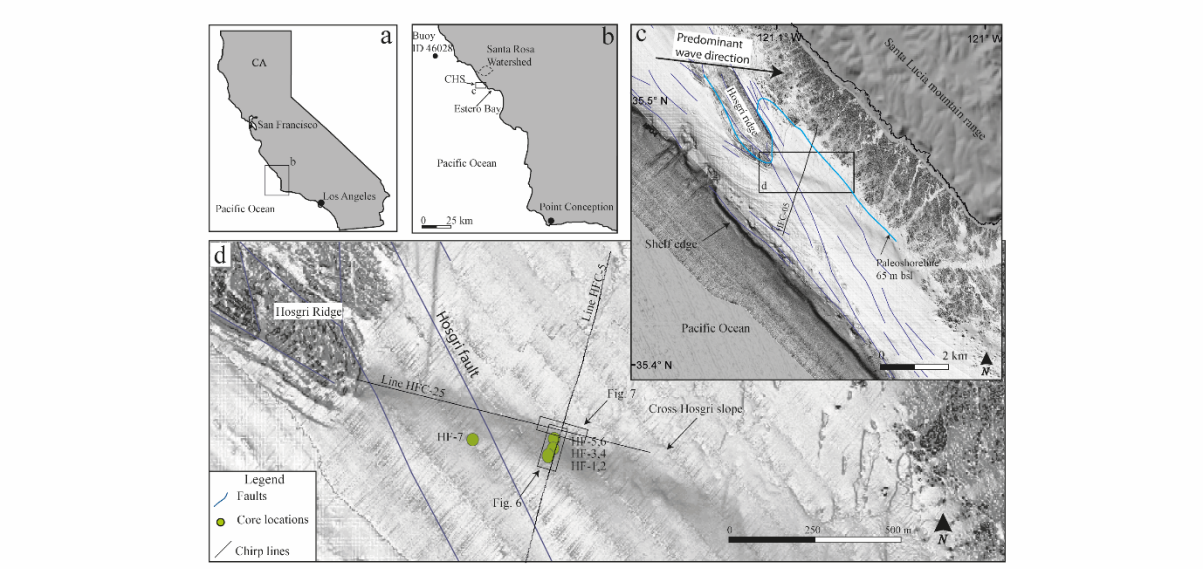

801

802 **Figure 1:** (a) Map of California highlighting the study area. (b) Location in California of the
803 study area. (c) Shaded relief of the continental shelf in the study area based on multibeam
804 bathymetry (California State University Monterey Bay Sea Floor Mapping Lab [CSUMB],
805 2012; Hartwell et al., 2013). (d) Shaded relief of the study area, highlighting the location of
806 cores, previously mapped faults (blue lines), and the chirp profile.

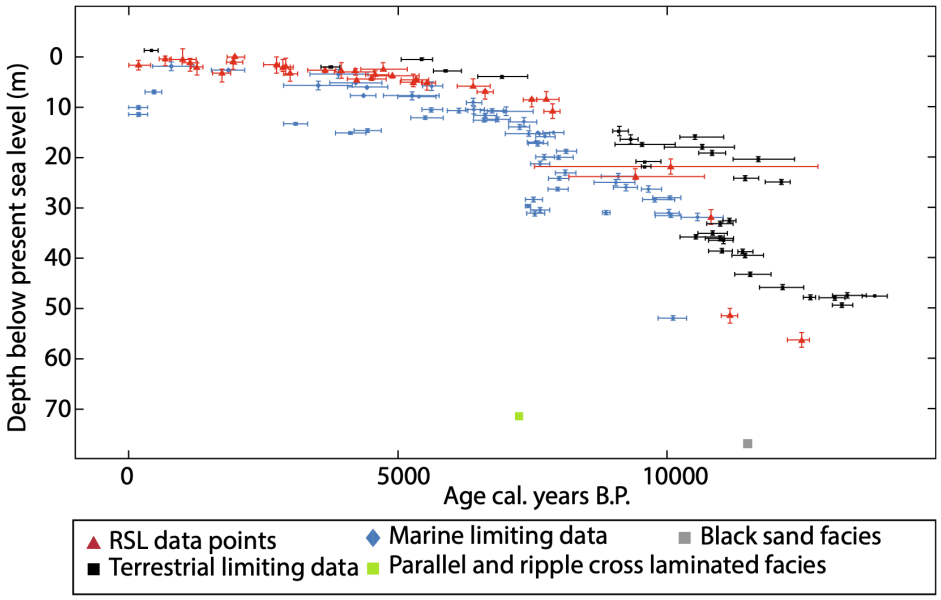

807

808 **Figure 2:** The age and elevation of radiocarbon ages obtained from the parallel and ripple

809 cross laminated facies (green square) and the black sand facies (gray square) plotted

810 alongside the relative sea-level constraints for southern California compiled by Reynolds and

811 Simms (2015, Fig. 2).

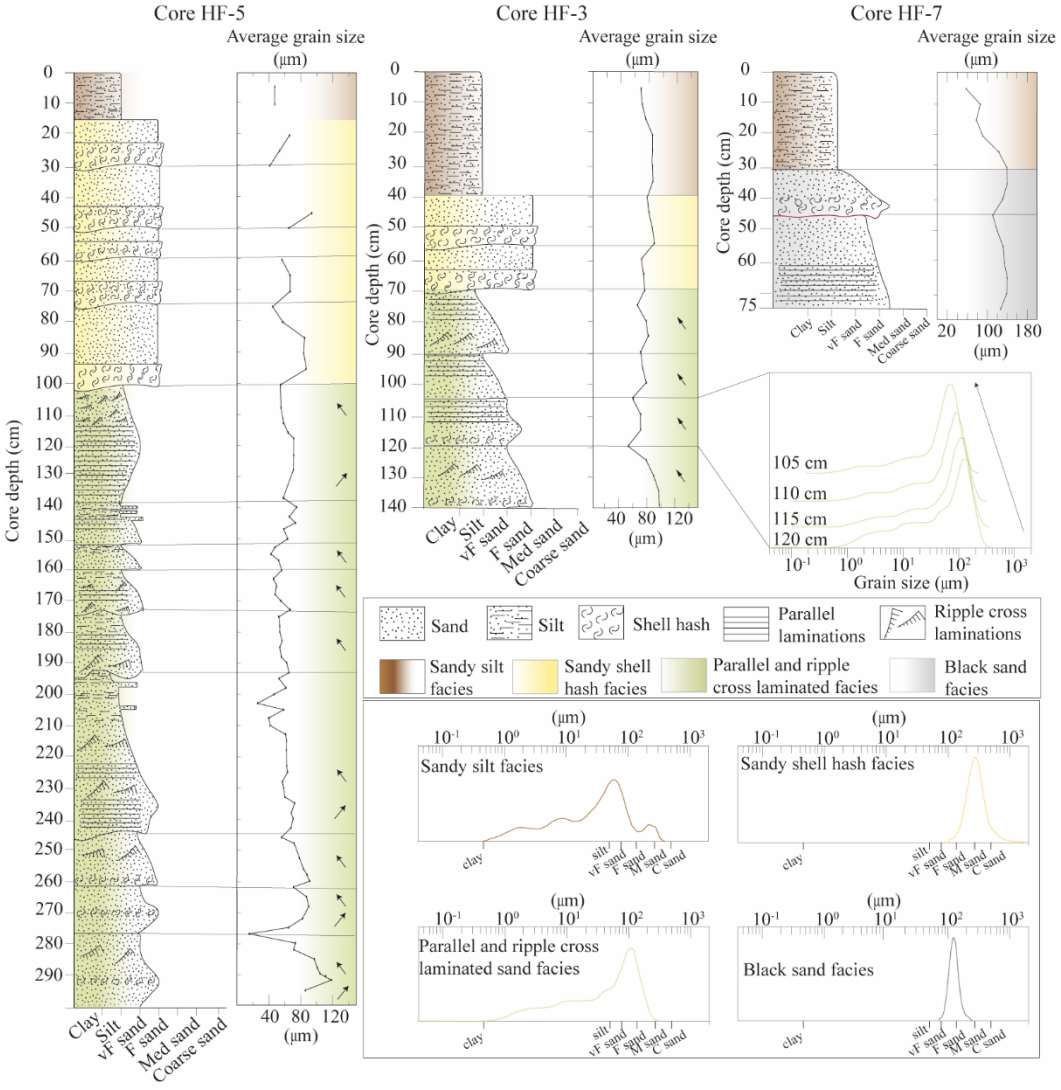

812

813 **Figure 3**: Stratigraphic profiles, average grain size, and representative facies grain size

814 distributions (bottom panel) for cores HF-3, HF-5, and HF-7.

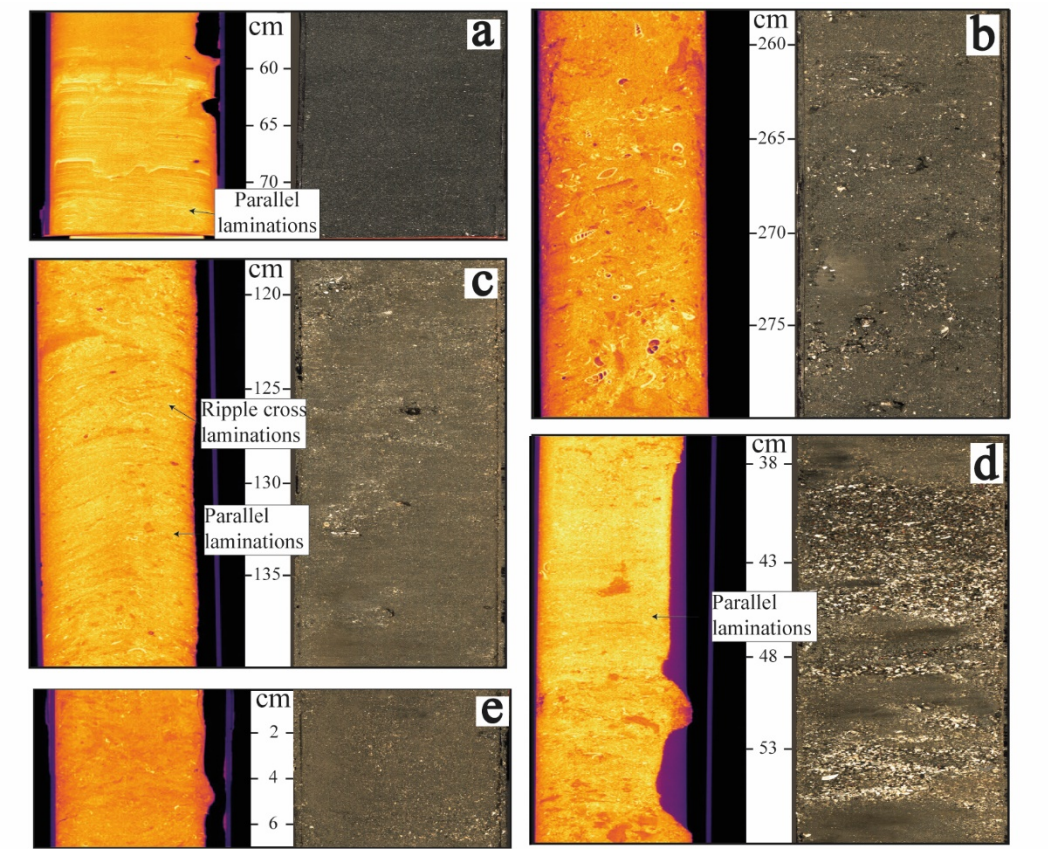

Figure 4: Photographs (right) and Computed Tomography (CT) scans (left) of the sedimentary facies identified in the cores. a) Black sand facies. Photograph and CT scan from core HF-7 at depth 75-55 cm. b) Parallel and ripple cross laminated facies, showing the coarsening upward portion. Photograph and CT scan from core HF-5 at depth 280-258 cm. c) Parallel and ripple cross laminated facies, showing the fining upward portion. Photograph and CT scan from core HF-5 at depth 140-118 cm. d) Sandy shell hash facies. Photograph and CT scan from core HF-5 at depth 58-36 cm. e) Sandy silt facies. Photograph and CT scan from core HF-7 at depth 7-0 cm.

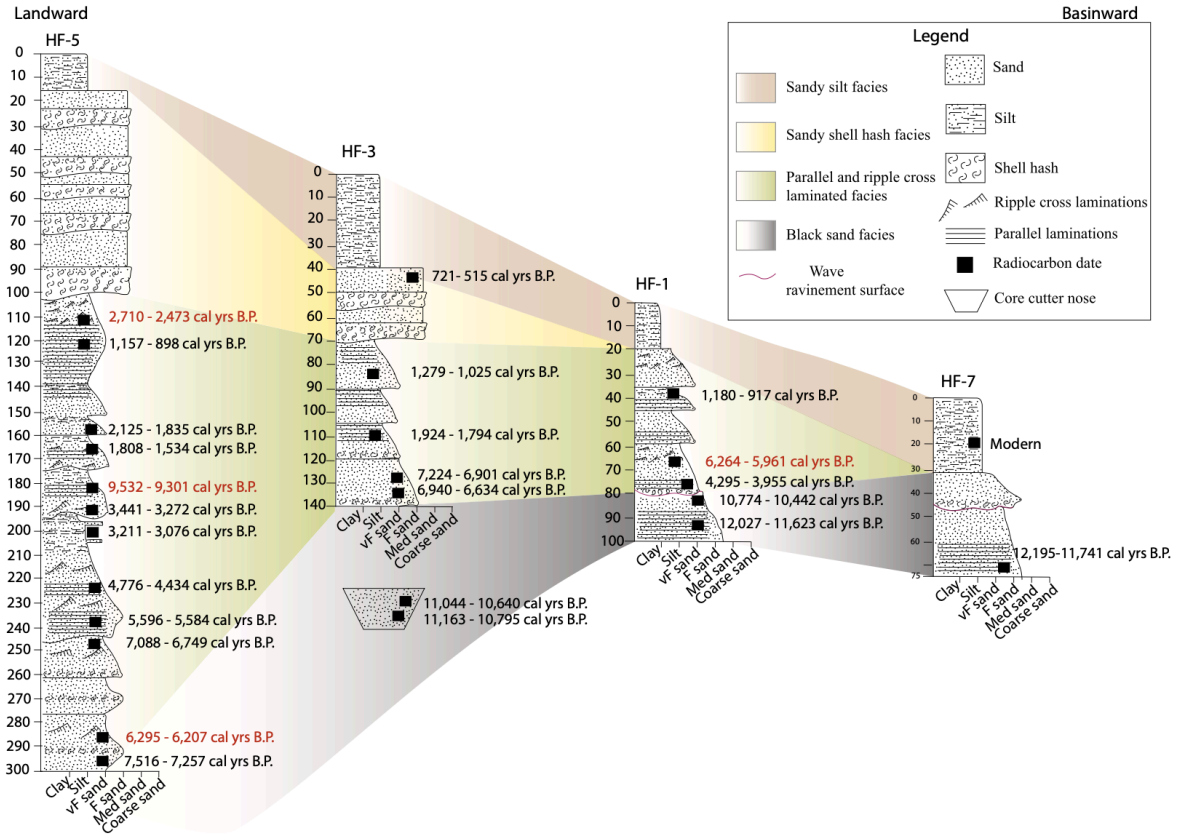

825

826 **Figure 5:** Stratigraphic logs and correlations from four cores collected on the Cross Hosgri

827 Slope (CHS), along with radiocarbon ages. Dates marked in red are interpreted as out of

828 sequence ages and highlighted by * in Table 2.

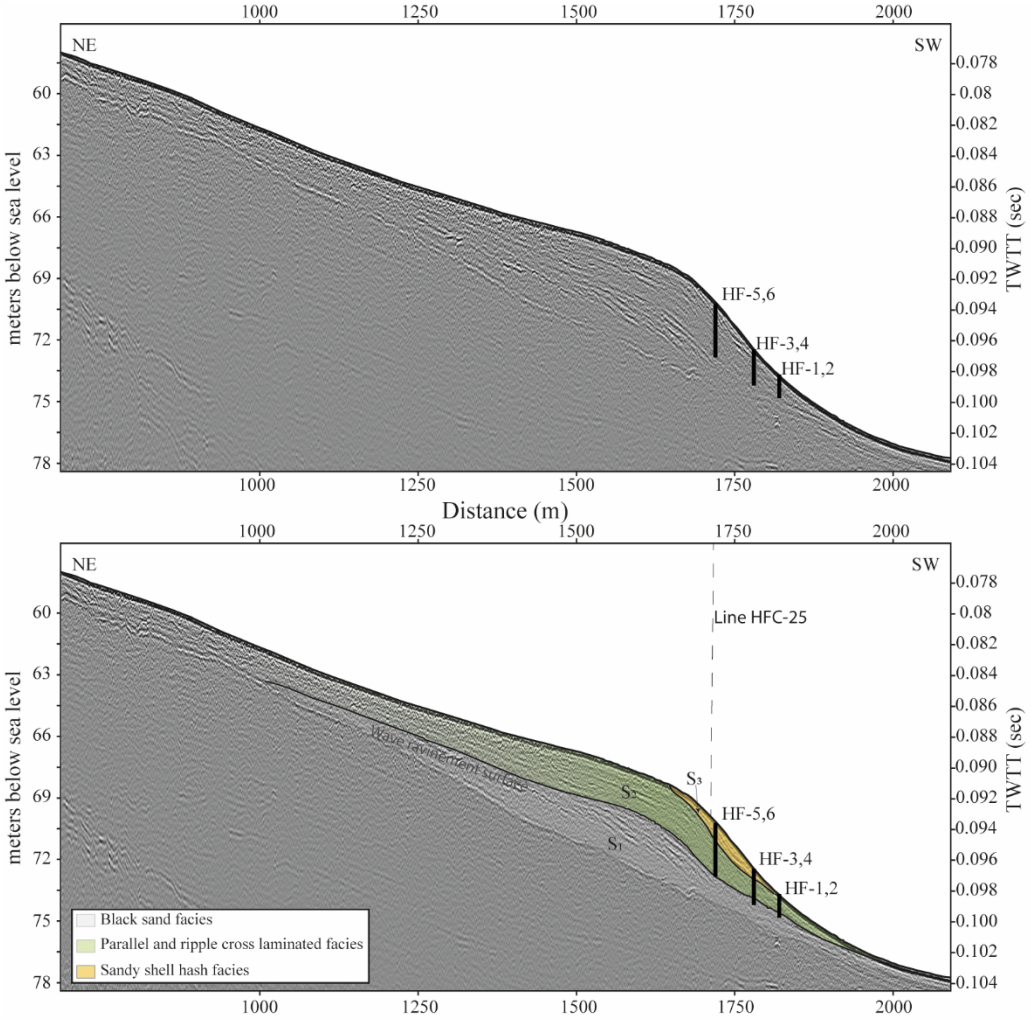

Figure 6: Seismic line HFC-5 across the Cross Hosgri Slope (CHS; see Fig. 1 for location). Upper profile is shown without interpretations. Lower profile shows seismic units S_1 (gray), coinciding with the black sand facies, S_2 (green) comprised of the parallel and ripple cross laminated facies and the sandy silt facies, and S_3 (yellow) comprised of the uppermost portion of the sandy shell hash facies and the silty sand facies. VE ~ 32.

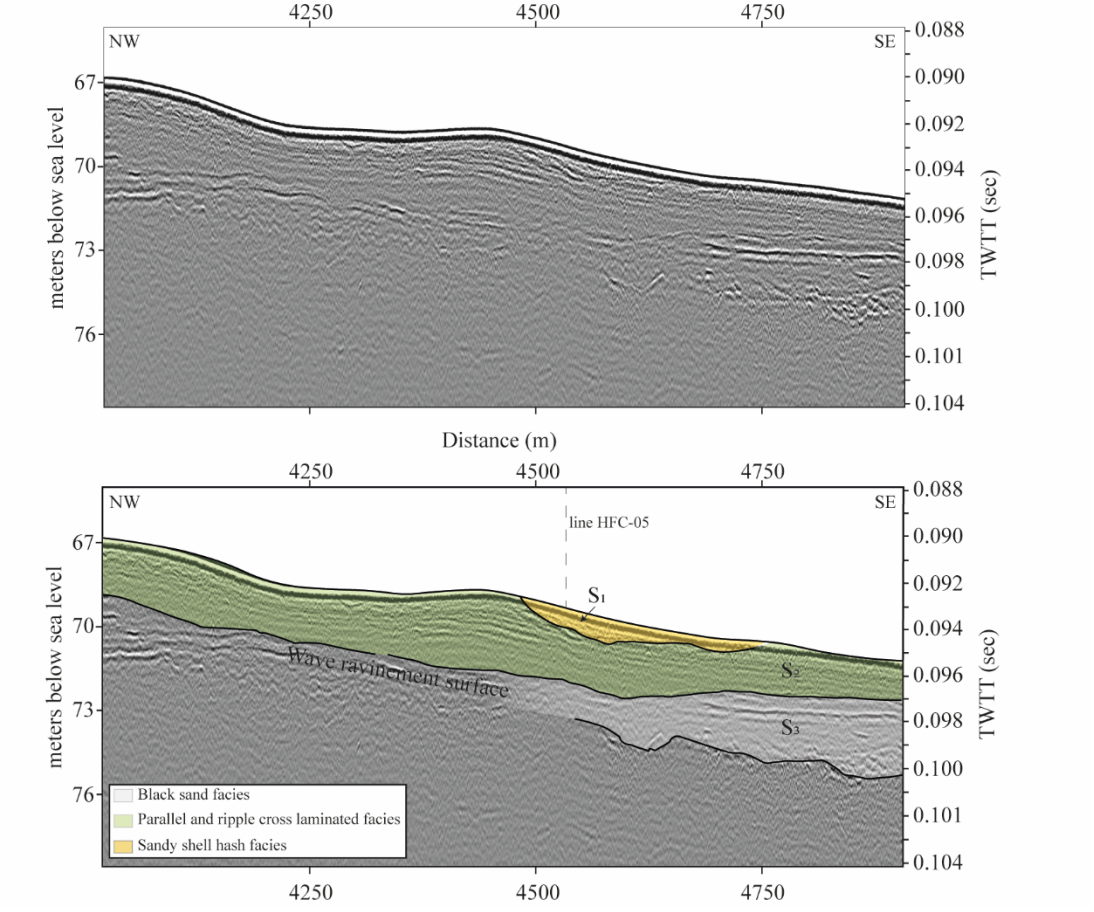

835

836 **Figure 7**: Seismic line HFC-25 along strike of the Cross Hosgri Slope (CHS; see Fig. 1 for
837 location). Upper profile is shown without interpretations. Lower profile shows seismic units
838 S_1 (gray), coinciding with the black sand facies, S_2 (green) comprised of the parallel and
839 ripple cross laminated facies and the sandy silt facies, and S_3 (yellow) comprised of the
840 uppermost portion of the sandy shell hash facies and the silty sand facies. VE ~34.

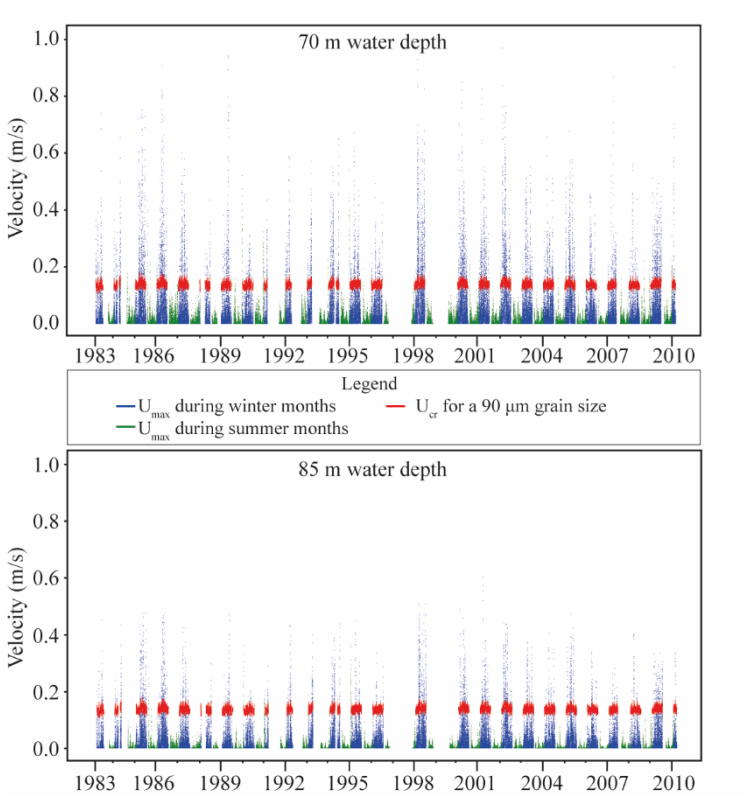

841

842 **Figure 8:** Values of U_{max} and U_{cr} calculated from wave data northwest of Estero Point
843 (NOAA.gov, station ID: 46028) from 1983 to 2010. Top panel shows U_{max} and U_{cr} at 70 m
844 water depth during winter (October-March) and summer (April-September) months. Bottom
845 panel shows U_{max} and U_{cr} at 85 m water depth during winter (October-March) and summer
846 (April-September) months.

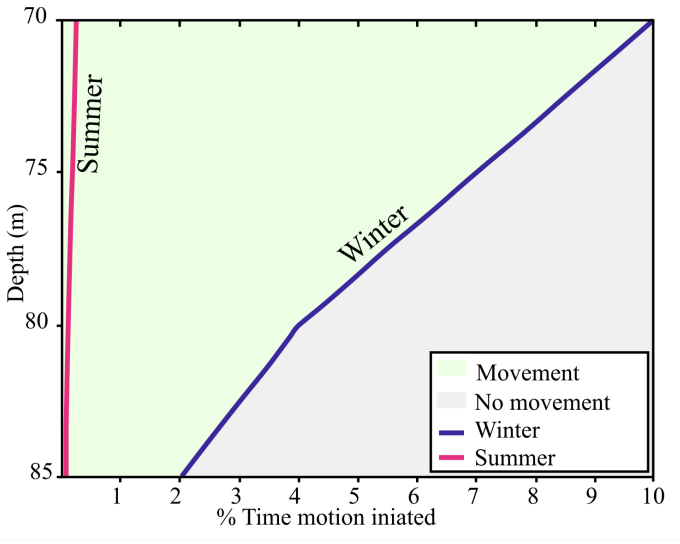

847

848 **Figure 9:** Plot showing % time during which $U_{max} > U_{cr}$ for a grain size of 90 μm and how
849 this condition varies with increasing depth, both in summer conditions and winter conditions.

850

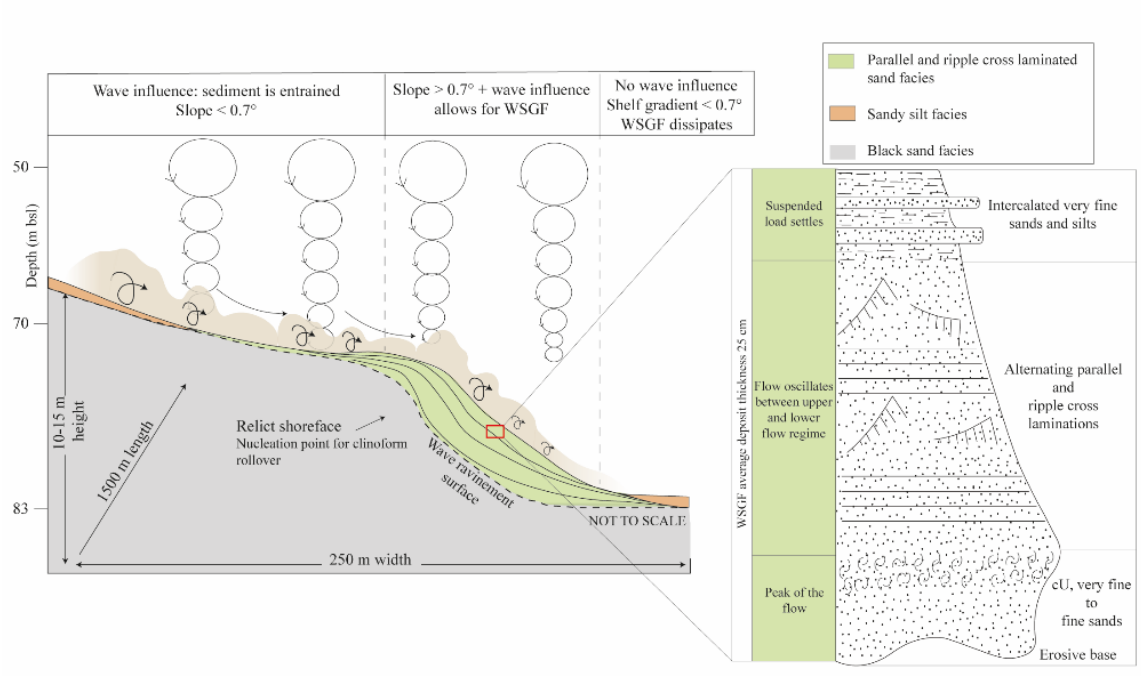

851

852 **Figure 10**: Diagram depicting mode of sediment transport and deposition along the Cross
853 Hpsgri Slope (CHS) subaqueous clinoform in a sandy environment with no direct riverine
854 input (left). Facies model for the wave-supported gravity flows (WSGF) deposit along the
855 foreset of the subaqueous clinoform (right).

856

Core #	Length (m)	Depth (m)	Latitude	Longitude
HF-1	0-97	82	35 28.5902	121 04.4682
HF-2	0-109	80	35 28.5902	121 04.4682
HF-3	0-143	73	35 28.6101	121 04.4610
HF-4	0-172	73.5	35 28.6101	121 04.4610
HF-5	0-297	71.6	35 28.6407	121 04.4502
HF-6	0-260	72	35 28.6407	121 04.4502

HF-7	0-77	81	35 28.6440	121 04.8010

857

858 [1] Core lengths, water depths, and locations.

859

UCIAMS #	Core	Depth (cm)	Material/species	D^{14}C ‰	±	^{14}C age	±	Calibrated age (Cal years B.P.)
254929	HF-1	46	*Amphissa versicolor*	-186.7	1.3	1660	15	1180-917
254931	HF-1	61	*Neverita lewiisi*	-519.68	1.0	5890	20	**6264-5961***
254930	HF-1	80	*Amphissa versicolor*	-408.7	1.3	4220	20	4295-3955
254932	HF-1	90	*Clathurella canfieldi*	-705.8	0.6	9825	20	10774-10442
254936	HF-1	97	*Truncatella californica*	-734.9	0.6	10665	20	12027-11623
260440	HF-2	103.5	Gastropod	-730.1	0.7	10520	25	11808-11386
260441	HF-2	106	Gastropod	-712.3	0.7	10010	20	11085-10714
246214	HF-3	Cutter nose	*Callianax baetica*	-710.30	0.7	9950	20	11044-10640
230405	HF-3	VC cutter nose	*Gastropod*	-714.6	0.9	10075	25	11163-10795
243289	HF-3	137	*Amphissa versicolor*	-555.3	0.8	6510	15	6940-6634
230406	HF-3	131	*Gastropod*	-568.3	1.1	6750	25	7224-6901
243298	HF-3	110	Wood	-213.6	1.2	1930	15	1924-1794
243290	HF-3	80	Bivalve	-196.2	1.4	1755	15	1279-1025
243291	HF-3	40	*Amphissa versicolor*	-140.9	1.5	1220	15	721-515
260442	HF-4	154	*Turritella cooperi*	-683.2	0.7	9235	20	10035-9620
260443	HF-4	171.5	Gastropod	-679.2	0.7	9135	20	9857-9524

243299	HF-5	115	Wood	-265.7	1.2	2480	15	**2710-2473***
243292	HF-5	122	*Amphissa versicolor*	-183.2	1.3	1625	15	1157-898
254938	HF-5	155	*Amphissa versicolor*	-267.4	1.2	2500	15	2125-1835
254933	HF-5	166	*Amphissa versicolor*	-243.7	1.2	2245	15	1808-1534
254935	HF-5	175	*Callianax baetica*	-670.7	0.6	8920	20	**9532-9301***
254945	HF-5	180	Wood	-323.6	1.1	3140	15	3441-3272
254944	HF-5	199	Wood	-309.4	1.1	2975	15	3211-3076
254937	HF-5	222	*Amphissa versicolor*	-434.4	0.9	4575	15	4776-4434
246230	HF-5	233	Wood	-451.8	0.9	4830	15	5594-5484
243293	HF-5	255	*Callianax baetica*	-561.5	0.7	6625	15	7088-6749
243300	HF-5	287	Wood	-492.6	0.9	5450	15	**6295-6207***
260444	HF-5	296	*Turritella cooperi*	-586.1	0.9	7085	20	**7516-7257**
254934	HF-7	20	*Amphissa versicolor*	8.2	1.6	Modern		
246207	HF-7	70	*Callianax baetica*	-737.6	0.7	10750	25	12195-11741

[2] Radiocarbon ages obtained during this study. Ages in bold and marked by an asterisk indicate the ages interpreted as out of sequence.

Facies	**Sedimentary structures**	**Other features**	**Mean grain size**	**Deposition mode/Interpreted environment**	**Occurrence (yrs B.P.)**
Black Sand	-Well developed parallel laminations	-Shell fragments <5% -Well sorted, clean sand	130 µm	-Inner shelf -Shoreface	~ 12 – 10 ka

Parallel and ripple cross laminated facies	-cU then fU sequences -Ripple cross laminations -Parallel laminations	-Shell fragments 20-25%	90 µm	-WSGF -Distal -Mid shelf slope	~ 7 ka- 900 ybp
Sandy shell hash	-Faint parallel laminations	-Shell fragments ~35%, up to 5 cm in size	330 µm	-Storm wave resuspension -Proximal -Mid shelf slope	~ 7 ka- 900 ybp
Sandy silt	-Massive	-Shell fragments 3-5%	40 µm	-Suspension settling -Mid shelf	< 700 ybp

[3] Description and interpretation of the depositional regimes and environments of the four facies identified in the cores and their approximate age.